PAPER • OPEN ACCESS

The metrological structural resolution for dimensional x-ray CT: analysis of the comparability between the CEB and the PBS method

To cite this article: René Laquai *et al* 2023 *Meas. Sci. Technol.* **34** 084002

View the article online for updates and enhancements.

The metrological structural resolution for dimensional x-ray CT: analysis of the comparability between the CEB and the PBS method

René Laquai[1,*] ●**, Jens Illemann**[2]**, Markus Bartscher**[1] **and Ulrich Neuschaefer-Rube**[1] ●

[1] Multisensor Coordinate Metrology, Physikalisch-Technische Bundesanstalt, Braunschweig, Germany
[2] X-ray Radiometry, Physikalisch-Technische Bundesanstalt, Berlin, Germany

E-mail: rene.laquai@ptb.de

Abstract

The metrological structural resolution (MSR) describes the size of the smallest surface feature that can be measured dimensionally with a given accuracy. Several methods to determine the MSR for dimensional x-ray CT (dXCT) have been proposed in the past, two of which are compared and related in this publication, i.e. the curved-edge based (CEB) and the profile-based spectral (PBS) method. Both methods consider the surface structure as being described by a single surface on the relevant local scale and are also suitable for the application to optical or tactile coordinate measurement systems (CMSs). The CEB method evaluates the radii of circular shapes to determine the width of the Gaussian filter that describes the filtering of the surface by the CMS. The PBS method evaluates the instrument transfer function (ITF) determined by means of the measurement of a surface profile with a broad-band spatial frequency spectrum with a finite cut-off frequency. The PBS method yields the threshold wavelength for which the amplitude of the ITF drops below a certain level. While the resulting quantities of the two methods are very different they evaluate the same characteristic of the CMS. In this publication an analytical relation between those results is derived and shown to exist which is used to define the MSR. Simulated CT scans as well as dXCT measurements are performed to verify this relation. The results for the MSR obtained from both methods are consistent and deviations to the expectations based on theory are within a reasonable range.

Keywords: industrial CT, dimensional metrology, metrological structural resolution

(Some figures may appear in colour only in the online journal)

---

* Author to whom any correspondence should be addressed.

1. Introduction

The resolution is an important system parameter for coordinate measuring systems (CMSs) using the principle of x-ray computed tomography for dimensional measurements (dXCT) but is not conclusively standardised yet. The current definition of the resolution according to the International Vocabulary of Metrology is based on the detectability of a change in the measured quantity [1]. However, this definition is not sufficient regarding dimensional metrology, since for this application not only the detection of geometries is of interest but more importantly the ability to measure their dimensions with sufficiently small measurement uncertainty. Therefore, the metrological structural resolution (MSR) is proposed as a definition for a resolution characteristic for dXCT. The MSR describes the smallest surface feature of a measured surface that can be measured dimensionally with a given accuracy. In the context of this publication a surface feature is part of a single surface on a local scale, i.e. cases of multiple surfaces are excluded (no lamellae, pores, or gaps). Furthermore, the main extend of the feature is perpendicular to the surface to be analysed. Thus, the here defined and analysed characteristic is different from characteristics referred to as MSR in other publications, e.g. [2] where the surface features are described by multiple surfaces.

The two methods used in this publication will be described in the upcoming International Organization for Standardization (ISO) Technical Report on structural resolution of dXCT (ISO TR 11335) to measure the single-surface MSR. Both methods consider the entire dXCT process chain, consisting of acquisition, reconstruction, and surface determination, as a black box evaluating only a set of measured coordinates on the object's surface. Both methods have been individually proposed and validated for their suitability to determine the single-surface MSR [3–5].

Each method has its own advantages and might be more suitable for certain applications. The profile based spectral (PBS) method evaluates the amplitude of a spatial frequency spectrum to directly measure the instrument transfer function (ITF). Therefore, the resulting MSR does not include a model assumption for the filtering of the CMS. Further, every point of the measured profile contributes to the result as it is gained by a Fourier transform of the entire profile. Thus, the result is more strongly averaged yielding more stable and reliable results. The ITF is also well established in other fields of science for resolution statements, e.g. optics, so that its use in dimensional metrology possibly increases acceptance. The major disadvantage is that it is very difficult to produce reference standards with profiles containing spatial frequencies large enough to reach the resolution limits of state-of-the-art high-resolution measurement systems.

The curved-edge based (CEB) method evaluates the MSR by evaluating the radii of circular shapes. For this method it is easier to produce reference standards with sufficiently small radii to evaluate state-of-the-art high-resolution measurement systems and, additionally, it is possible to distinguish between convex and concave curvatures. However, the MSR is only measured indirectly and an assumption for the

filtering of the CMS must be made, usually that of a Gaussian filter. Additionally, the result is greatly impacted by the form of the circles and large form deviations lead to errors or instabilities of the circle fit. Also, the accuracy of the circle fit depends on the number of points used and depending on the measurement the actual curvature can be represented by rather few points making the fit less reliable. Therefore, if possible, each point of the measured profile should be determined by averaging measurement points perpendicular to the profile.

For the methods to be introduced to standardization their results must be validated. Therefore, it is useful to have compatible methods available which can be used interchangeably depending on the specific application. Moreover, in the upcoming ISO TR 11335 the two methods are stated to quantify the same characteristic of a dXCT system. Therefore, there must be a relation between the results of two methods and they must yield equivalent values for the MSR.

The purpose of this publication is to show that such an analytical relation between the results of the two methods exists and to compare the values for the MSR obtained from the two methods. While the comparison is done on the example of dXCT, the outcome of the comparison could also be transferred to other CMSs using different principles as both methods have been successfully applied to tactile and optical CMSs [3, 5].

2. Methods for determining the MSR

2.1. Curved-edge-based (CEB) method

With the CEB method [3] the MSR is determined by evaluating the radii of circular concave or convex shapes. The measured radii deviate from their calibrated value due to the filtering by the CMS measurement process as shown in figure 1. The filter is assumed to have the shape of a Gaussian function. Ideally the curvature of the reference standard is a rectangular function, i.e. the profile consists of a straight-line segment followed by a circular segment and another straight-line segment. The first derivative of the profile is continuous and the projections of the straight-line segments to the baseline should be longer than $3 \cdot 2\sigma$, where the 2σ value used here is an estimate based on experience or a specification value of the CMS under study. To ensure accurate radius fitting and the assessment of the structure as single surface the following criteria for the opening angle α and the radius R of the circular segment should be met with respect to the expected width 2σ of the Gaussian filter

$$30° \leqslant \alpha \leqslant 60° \text{ and } 0.2 \cdot 2\sigma \leqslant R \leqslant 2 \cdot 2\sigma \qquad (1)$$

The profile is evaluated by fitting a circle to the surface points of the arc of the convex or concave shape using the opening angle α as a constraint for the selected points. This way the measured radii $\tilde{R}$ are obtained. In this notation the tilde on top of a symbol denotes a measured quantity. With the calibration values of the radii R the dimensionless ratio $\tilde{r} = \tilde{R}/R$ is calculated and the dimensionless Gaussian filter
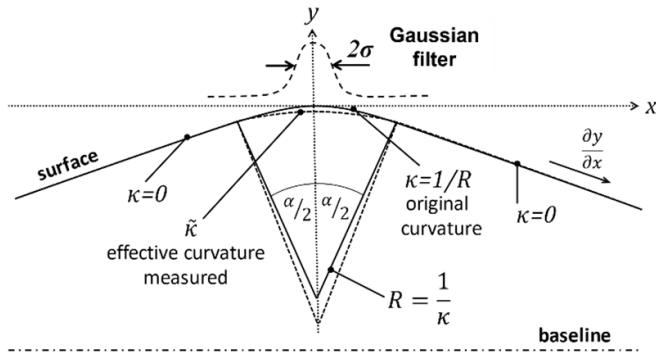
Figure 1. CEB method: a circular curved edge of curvature κ with opening angle α is convolved with a Gaussian filter of size 2σ and causes a measured curvature $\tilde{\kappa}$. (Adapted from [3].)

width $\tilde{s} = 2 \cdot \tilde{\sigma}/R$ is determined using a look-up table or the numerical approximation of equation (2) (both shown in [3])

$$\tilde{r} \cong 1 + l \cdot e^{-1.06/l} \text{with } l = \frac{0.628 \cdot \tilde{s}}{\tan \alpha/2}. \quad (2)$$

The result of the CEB method is the standard deviation of the Gaussian describing the filtering by the CMS which will be denoted σ_{CEB} henceforth. The MSR is then given as $m \cdot \sigma_{\text{CEB}}$ with m being a constant factor which is derived from the analytical relation between the CEB and PBS methods as will be shown in section 2.3.

2.2. Profile-based spectral (PBS) method

The PBS method [5] is based on the analysis of a profile featuring a broad-band spatial frequency spectrum with a finite cut-off frequency. This approach observes the surface amplitude response over the spatial frequency through the CMS and yields the ITF. The surface profile $r(z)$ is described as the sum of sine waves with dimensionless integer wave number k, up to a given limit $k_{\max}$, positive amplitudes A_k, and phase shifts φ_k

$$r(z) = \sum_{k=1}^{k_{\max}} A_k \cdot \sin\left(\frac{2\pi \cdot k \cdot z}{L} + \varphi_k\right). \quad (3)$$

The spectral amplitude is ideally equal for all wave numbers and the phase of the wave components is designed to be random and uncorrelated. Further, the profile should be longer than its period length L. More details on the design of such a profile can be found in [5]. An example of such a surface profile and the corresponding spatial frequency spectrum is shown in figure 2.

To analyse the profile a discrete Fourier transform (DFT) is applied, and the absolute value of the result is divided by the calibrated amplitude spectrum of the profile for normalisation, yielding the measured ITF. The result of the PBS method is the threshold wavelength $\lambda_{\text{thr}}^{(q)}$ for a given amplitude limit $0 < q < 1$ of the measured ITF. $\lambda_{\text{thr}}^{(q)}$ is defined by the dimensionless wave number $k_{\text{thr}}^{(q)} = L/\lambda_{\text{thr}}^{(q)}$ which is the smallest wave number for which the ITF value is still within
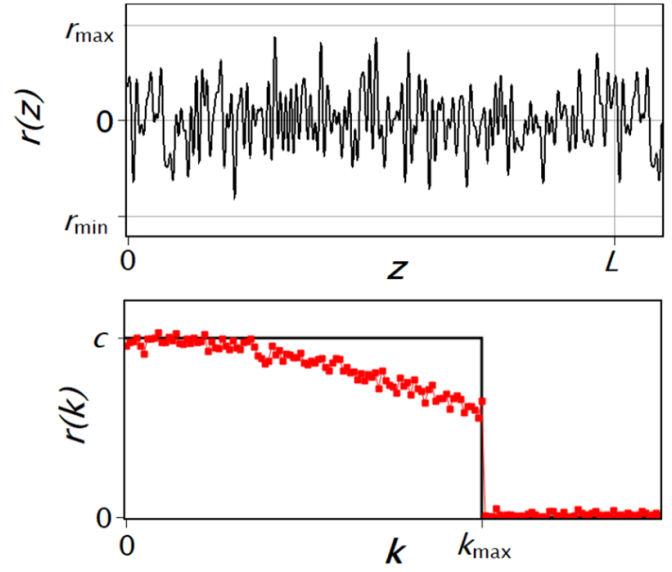

Figure 2. PBS method: example profile $r(z)$ (top) with an ideal flat amplitude spectrum $r(k)$ (bottom, black) with limited bandwidth. Real measurements show decreasing amplitudes for higher wavenumbers and noise (bottom, red).

the amplitude limit interval $[q, q^{-1}]$. For the case of CT, a value of $q = 0.8$ is recommended. A numerical analysis shows that in this case the height of a rectangular surface structure with a width equivalent to $1/2 \cdot \lambda_{\text{thr}}$ can be measured with an accuracy of more than 98 %. This threshold wavelength will henceforth be denoted λ_{PBS}.

To avoid the influence of drift effects and form deviations of the reference standard, a reference standard should be used for which the following condition is fulfilled:

$$L > \lambda_{\text{thr}}^{(q)} \cdot 0.2 \cdot k_{\max}. \quad (4)$$

2.3. Relation between CEB and PBS method

The quantities σ_{CEB} and λ_{PBS} obtained from the two methods are complementary and an analytical relation between them exists. This relation is derived assuming that the filtering of the surface by the CMS is described by a Gaussian function

$$g(x) = A \cdot e^{-\frac{x^2}{2 \cdot \sigma^2}}. \quad (5)$$

Here, A is a constant defining the amplitude and σ is the standard deviation of the Gaussian. This standard deviation would be the result of the CEB method. To relate this quantity to the result of the PBS method the wavelength must be found for which the amplitude of the wave is reduced to q times its original amplitude by the filtering process, where q is the threshold chosen for the PBS method. The filtering process is described by a convolution of the wave function with the Gaussian filter which is equivalent to a multiplication in Fourier space. Thus, the amplitude of the ITF is modified by multiplication with the Fourier transform of the Gaussian

$$g(x) = \int g(k) \cdot e^{-2\pi i k x} dx \quad (6)$$

$$g(k) = A' \cdot \mathrm{e}^{-2\pi^2\sigma^2 k^2}. \qquad (7)$$

Here, k is the wave number of the wave convoluted with the Gaussian filter. Because the factor A' is independent of k, the exponential term is defined as the threshold value q

$$q \underset{=}{\mathrm{def}} e^{-2\pi^2\sigma^2 k^2}. \qquad (8)$$

Rearranging yields the wave number k as a function of σ and q and with the relation $k = 1/\lambda$ we arrive at the relation between the wavelength λ and the standard deviation σ of the Gaussian filter

$$\lambda = \sigma \cdot \sqrt{\frac{2\pi^2}{\ln q^{-1}}}. \qquad (9)$$

Since the MSR shall represent the smallest width of a surface feature whose height can be measured with a certain accuracy, it is defined as one peak or valley of the respective wave, i.e. half of its wavelength

$$\mathrm{MSR} = \frac{1}{2}\lambda_{\mathrm{PBS}}^{(q)} = \sigma_{\mathrm{CEB}} \cdot \sqrt{\frac{\pi^2}{2\ln q^{-1}}}. \qquad (10)$$

This represents a linear relation between the threshold wavelength λ_{PBS} and the standard deviation of the Gaussian filter σ_{CEB}. For a threshold value of $q = 0.8$ the term $\sqrt{\frac{\pi^2}{2\ln 0.8^{-1}}} \cong 4.70$.

3. Experimental verification

3.1. Test objects

Simulations and CT measurements are performed on CEB and PBS reference standards of two sizes manufactured from Fe/Cu/Pb-free aluminium.

The large and small PBS reference standards are angular segments of $\sim$22° of hollow cylinders with diameters of 36 mm and 18 mm and lengths of 12.7 mm and 4.0 mm, respectively. The respective profile is extended over the entire outer circumference of the cylinder and manufactured by diamond turning. The profiles of the two PBS reference standards have period lengths of $L = 10$ mm and $L = 2$ mm with the amplitude of the wave numbers $1 \leqslant k \leqslant 100$ set to a fixed value and the amplitude of wave numbers $k > 100$ set to zero. The corresponding phase of each wave was generated by seeded random numbers to obtain a profile with sufficiently large radii of curvature and small slopes to allow manufacturing as well as tactile and optical measurements. Thus, the bandwidth is limited to 100 waves per period length. Further details on the PBS reference standards can be found in [5].

The large and small CEB reference standards are also angular segments of $\sim$22° of hollow cylinders with diameters of 36 mm and 18 mm and lengths of 12.7 mm and 3.0 mm, respectively. The profiles are also extended over the entire outer circumference of the cylinder and manufactured by diamond turning. The profiles consist of four concave and four convex circular shapes each with an opening angle of
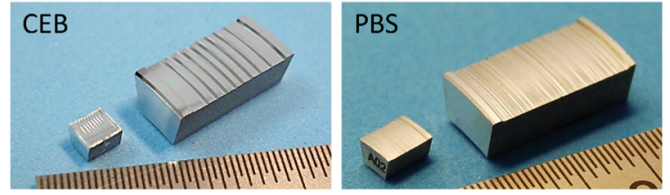

Figure 3. Photographs of the CEB and PBS reference standards.

$\alpha = 40°$. For the larger reference standard, the nominal radii are 0.05 mm, 0.1 mm, 0.2 mm, and 0.5 mm and for the smaller reference standard 0.005 mm, 0.01 mm, 0.02 mm, and 0.05 mm. Photographs of the reference standards are shown in figure 3. Both PBS and the large CEB reference standards have been calibrated on the high-resolution tactile scanner [6] of the 'Physikalisch-Technische Bundesanstalt' (PTB) while the small CEB reference standard has been calibrated on PTB's SIS Nanostation II non-contact atomic force microscope (AFM). For the simulation study STL-models of these reference standards were generated from the computer-aided design (CAD) models also used for diamond turning. Due to the finite sampling of the surface for the STL-models there exist minor deviations between the STL-models and the CAD-models which are accounted for by the normalisation by the ITF and the use of radii measured on the STL-models as reference. The manufacturing errors of the reference standards are small as shown in [5] so that the simulations with the STL-models obtained from the nominal CAD-model yield results comparable to the results of real measurements under similar conditions.

3.2. Simulations

The relation between the PBS and CEB methods is verified first by a simulation study. The simulations are performed using the 'analytical RT inspection simulation tool (aRTist)' [7] developed and publicly distributed by the German 'Bundesanstalt für Materialforschung und -prüfung (BAM)'. One important limitation of the software is that it performs calculations only with single-float precision. The CT geometry is set up with a source-to-detector distance of 1200 mm and a source-to-object distance of 48 mm resulting in a voxel size of 8 μm. This geometry resembles approximately PTB's NIKON MCT225 system which was used for the actual dXCT measurements (see section 3.3). The reference standards were placed at an angle of 45° to the rotation axis. To exclude undefined influences on the MSR, the simulations were performed without noise, an ideal sensitivity of the detector, no blur of the detector, no scattering, and monochromatic x-rays of 35 keV. The filtering was realized by variation of the focal spot size whose intensity distribution follows a Gaussian function. Size and shape of the focal spot were adjusted to closely match the focal spot observed in the actual dXCT measurements. Therefore, the projection simulations were performed with an elliptical focal spot using the full width at half maximum (FWHM) in vertical and horizontal direction determined on the CT system used for the

Table 1. FWHM of the three focal spot settings along the vertical and horizontal axis as observed in the dXCT measurements and used for simulations.

Configuration	Vertical FWHM	Horizontal FWHM	Avg FWHM
1	6.8 μm	13.4 μm	10.1 μm
2	29.9 μm	50.0 μm	40.0 μm
3	46.5 μm	79.4 μm	63.0 μm

measurements. The different configurations are summarized in table 1. Additionally, one projection simulation with an ideal point source was performed. The projection simulation with an ideal point source was performed by calculating only one ray from the source point to each detector pixel which may cause inaccuracies due to undersampling. An extended focal spot is represented by a random distribution of multiple source points, up to 150 points for the largest focal spot in this case, over the area of the focal spot. Therefore, undersampling effects present in the projection simulations performed with the point source do not occur in the projection simulations with extended focal spots.

Since the analytical relation presented in section 2.3 uses only one filter width, the focal spot size should be described by only one width as well. Therefore, the different configurations are represented by their average FWHM which is calculated as the arithmetic mean of the FWHM along the two axes. Additionally, the finite pixel grid of the detector induces another filtering step which cannot be avoided. To take both filtering steps into account, the focal spot size and the voxel size are combined to a quantity which will be denoted effective blur. To calculate the width $2\sigma_{\mathrm{eff}}$ of this effective blur the FWHM of the focal spot is first converted into its standard deviation as $\sigma = \mathrm{FWHM}/\sqrt{8\ln 2}$ [8] and the voxel size is converted into the respective standard deviation of a uniform distribution $\sigma_{\mathrm{voxel}} = \mathrm{voxel\ size}/\sqrt{12}$. The standard deviation of the effective blur is then calculated according to equation (11) which is valid for geometric magnifications $\gg 2$

$$\sigma_{\mathrm{eff}} = \sqrt{\sigma_{\mathrm{spot}}^2 + \sigma_{\mathrm{voxel}}^2} = \sqrt{\left(\frac{\mathrm{FWHM}}{\sqrt{8\ln 2}}\right)^2 + \left(\frac{\mathrm{voxel\ size}}{\sqrt{12}}\right)^2}. \tag{11}$$

All simulations are performed with 2000 projections along a circular trajectory and reconstructed using NIKON's CT Pro 3D 5.2.2 software without applying additional corrections and filtering.

3.3. Measurements

In addition to the simulation study, the relation between the PBS and CEB methods is verified also by a measurement study. CT measurements of the CEB and PBS reference standards were performed on PTB's NIKON MCT225 featuring a tungsten target. The x-ray tube voltage was set to 65 kV and a pre-filter of 0.1 mm aluminium was chosen. This yielded an x-ray spectrum with similar penetration strength as the monochromatic x-rays of 35 keV used in the simulation study. The

magnification was adjusted to achieve a voxel size of about 8 μm for both sizes of reference standards to match the settings of the simulations. All measurements were performed at an x-ray tube power of 7 W and the size of the focal spot was varied by defocussing the electron beam on the target by manipulating the current in the focussing coils of the x-ray tube. The resulting FWHM of the focal spot was determined by means of a test chart (JIMA RT RC-05) consisting of stripe patterns with well-defined widths and gaps. The FWHM of the focal spot is given by the pattern where an intensity modulation of 66.67% was observed [9]. In accordance with the observations in [9] the focal spot had an elliptical shape and the observed FWHMs along the vertical and horizontal axis are the same as used for the simulation study (table 1). For each focal spot size, the reference standard most suitable for the expected MSR was chosen. At the smallest focal spot size only the two small reference standards were measured, at the largest spot size only the two large reference standards, and at the intermediate spot size all four reference standards. The measurements were performed, as in the simulations, with 2000 projections along a circular trajectory and reconstructed using NIKON's CT Pro 3D 5.2.2 software without additional filtering. For all data sets the build-in polynomial beam hardening correction with parameter pre-set 2 was applied.

3.4. Data analysis

The surface of the reference standards was obtained from the volume data using the advanced surface determination of VG Studio MAX 3.0.3 with a search distance of four voxels and no further filtering of the starting contour. The starting contour was determined automatically as the iso-50 value between material and background peak of the grey value histogram. The resulting surfaces were registered to the axis of the cylinder as z-axis and an arbitrary point in the centre of the profile defining the zero point of the z-axis and the direction of the y-axis. The area containing the profile is then extracted as a region of interest and exported as point clouds with the tolerance parameter set to 0.5 μm.

These extracted surface coordinates were further processed as explained in [5]. This processing is comprised of the following four steps: (i) transformation of the data into cylinder coordinates, (ii) generation of a 2D profile from the 3D data. (iii) an adaptive filtering of the data that adjusts the lateral extend of the filter depending on the sparsity of data, and (iv) an equidistant resampling of the data using linear interpolation. The result is a smooth 2D profile that is averaged over the entire cylinder arc of the reference standard.

The profiles of the CEB reference standards were then analysed by fitting a circle to each circular convex and concave segment of the profile. Since the shapes contained only a segment of a circle an iterative fitting method is applied which uses the opening angle α of the circular segment as *a priori* knowledge and searches for a self-consistent solution. The radii of the fitted circles are then normalised by their respective calibrated value and the corresponding value of σ_{CEB} is determined from equation (2) together with the definition of $\tilde{s} = 2 \cdot \tilde{\sigma}/R$.

For the profiles of the PBS reference standards special care must be taken regarding the evaluated interval. The interval must exactly match the period length L because small deviations lead to systematic noise. A DFT was applied to the final filtered and resampled profile and divided by the calibrated profile to obtain the ITF. To determine the respective threshold wave number $k_{\mathrm{PBS}}^{(q)}$ a threshold value of $q = 0.8$ was chosen. Since any actual ITF obtained from measurement or simulation shows some degree of noise, the value of $k_{\mathrm{PBS}}^{(0.8)}$ is the smallest wave number with a normalised amplitude above 0.8. The threshold wavelength is then determined as $\lambda_{\mathrm{PBS}}^{(0.8)} = L/k_{\mathrm{PBS}}^{(0.8)}$. Here, as for all actual measurements, the wavenumber is based on the period length L and used as a dimensionless number.

4. Results and discussion

4.1. Simulations

The results for $2\sigma_{\mathrm{CEB}}$ of the simulated CT scans of the two CEB reference standards are presented in figure 4. The plot includes only results for radii for which the criterion of equation (1) is fulfilled.

The observed progression of $2\sigma_{\mathrm{CEB}}$ appears linear with a slope of 0.8 and an intersect of 6.5 at $2\sigma_{\mathrm{CEB}} = 0$ according to linear fitting. These values differ from a slope of 1 and an intersect at $2\sigma_{\mathrm{CEB}} = 0$ as would be expected under the assumptions that the effective blur $2\sigma_{\mathrm{eff}}$ as of equation (11) is the only source of blur and that the 2D blur in the projections is transformed linearly into the blur of the 3D volume. However, these assumptions are only approximately true. The simplified approach for calculating $2\sigma_{\mathrm{eff}}$ disregards other potential sources of blur, e.g. the reconstruction filter, limited number of projections, or surface determination, which are very difficult to quantify and are therefore excluded. Also, the reconstruction process itself is not linear and therefore the blur in the 3D volume is not necessarily equal to the blur in the 2D projection images. In addition, the limited single-float precision of the projection simulation could cause inaccuracies in the simulated data because the entire measurement process tends to become numerically ill-conditioned when very small features are considered.

The spread of the results for the different valid radii increases with increasing effective blur of the simulated extended focal spots from 2.6 μm at $2\sigma_{\mathrm{eff}} = 9.8$ μm to 16.7 μm at $2\sigma_{\mathrm{eff}} = 53.7$ μm. This behaviour is to be expected since a larger effective blur generally leads to a poorer quality of the profile. Therefore, the circle fit applied to determine the radii becomes less accurate. However, for the point source ($2\sigma_{\mathrm{eff}} = 4.6$ μm) again an increased spread is observed which is assumed to be caused by artefacts that originate from an undersampling of rays to each detector pixel during the projection simulation and the limited single-float precision of the respective computations.

It has also to be noted that the results for the 50 μm and 20 μm radii on the small reference standard are missing although they fulfil the criteria of equation (1). This is because the fits of the radii did not converge to a stable value due to
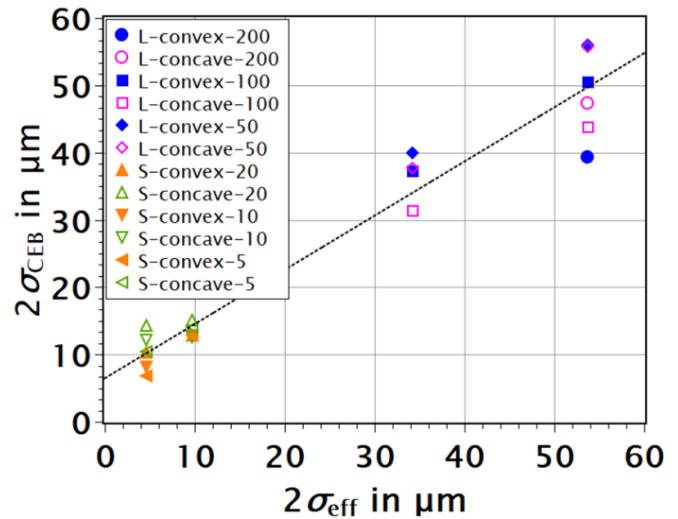

Figure 4. Plot of the width $2\sigma_{\mathrm{CEB}}$ of the Gaussian filter obtained from the simulations of the CEB reference standards against the calculated effective blur $2\sigma_{\mathrm{eff}}$ (equation (11)) resulting from the focal spot size and voxel size. Labels are denoted as follows: reference standard (L = large, S = small)—direction of curvature—nominal radius of assessed circle (in μm). The dotted line represents a linear fit though all data points.

the short length of the straight-line segments on both sides of the curved edge. For the subsequent comparison the arithmetic means of all valid values for $2\sigma_{\mathrm{CEB}}$ obtained at the same effective blur $2\sigma_{\mathrm{eff}}$ is calculated to obtain the final result for that $2\sigma_{\mathrm{eff}}$.

The ITFs obtained from simulated CT scans of the PBS reference standards are plotted in figure 5 for appropriate profile lengths, so that the condition of equation (4) holds. The ITFs obtained from directly analysing the STL-models, used for the simulations, are plotted as well showing almost the ideal flat spatial frequency spectrum of the design. The slight drop of the normalised amplitude is taken into account by the normalisation of the measured ITFs. For the large reference standard the ITFs obtained at an average focal spot size of 10.1 μm and with the point source do not drop below a normalised amplitude of 0.8 and the ITFs of the small reference standard obtained at an average focal spot size of 40 μm and 60 μm do so at wavenumbers $k_{\mathrm{thr}}^{(0.8)} < 0.2 \cdot k_{\mathrm{max}}$. Thus, the respective profiles yield no valid results.

As expected, the ITFs decrease more steeply for larger average focal spot sizes. The observed decrease of the ITFs is initially Gaussian-like and becomes nearly linear for larger wavenumbers.

The noise observed in the ITFs is very similar for all focal spot settings with exception of the point source. Considering the noise as the difference between the individual data points of the ITF and a smooth curve fitted to those points it can be evaluated by the residual sum of squares (RSS). For this purpose a Gaussian is fitted to the data in the interval of 20–100 wavenumbers keeping the centre and the y-offset fixed at 0. The resulting RSS for focal spot sizes of 10.1 μm, 40.0 μm, and 63.0 μm are 0.032, 0.022, and 0.030, respectively. For the point source the RSS is 0.093. This increased noise is assumed
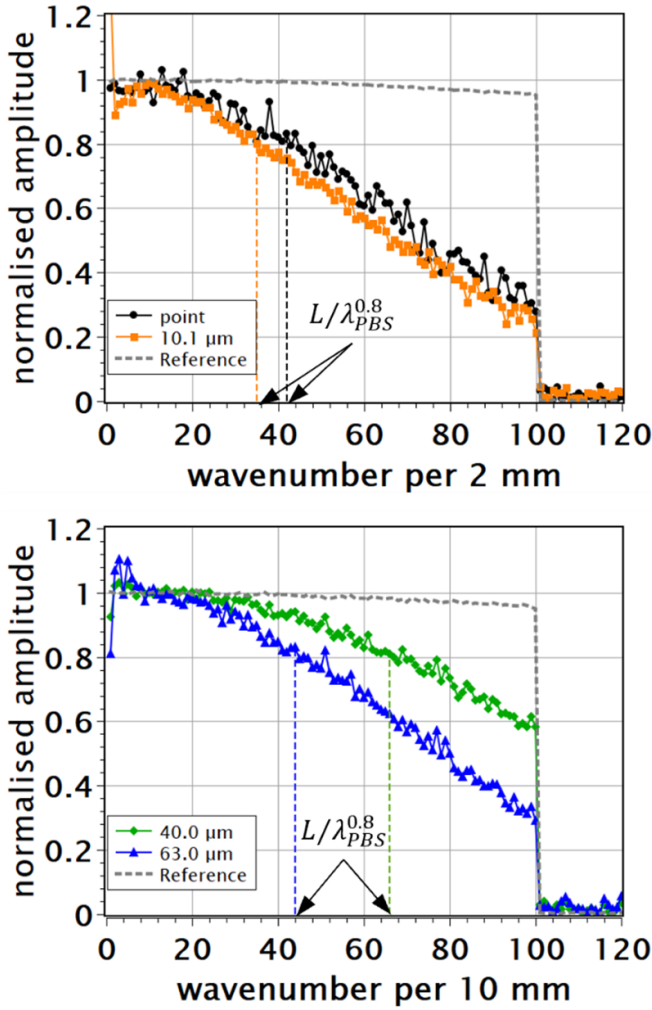
Figure 5. Plots of the ITFs obtained from simulations with different average focal spot sizes (point, 10.1 μm, 40.0 μm, and 63.0 μm FWHM diameter) of the small ($L = 2$ mm, top) and the large ($L = 10$ mm, bottom) PBS reference standards together with the direct evaluation of the input STL-models (dotted grey).

Table 2. Threshold wavelengths for the $q = 0.8$ threshold of the ITFs obtained for the respective focal spot size and effective blur and the used reference standard.

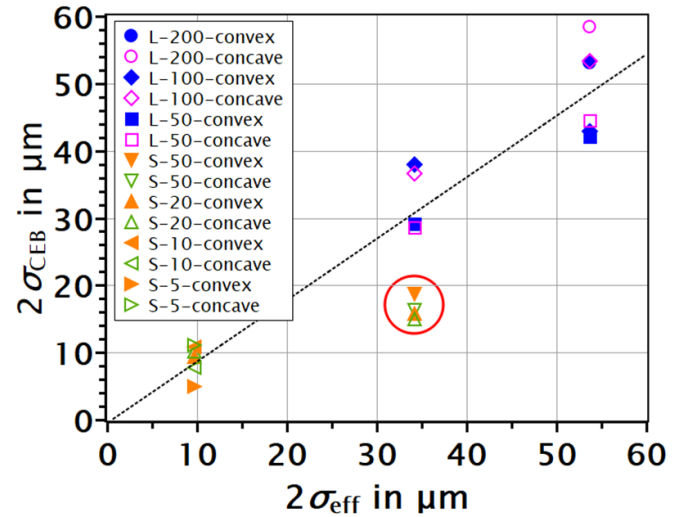| Avg focal spot size (FWHM)	Voxel size	$2\sigma_{\text{eff}}$	$\lambda_{\text{PBS}}^{0.8}$	Reference standard
Point	8.0 μm	4.6 μm	47.6 μm	Small
10.1 μm	8.0 μm	9.8 μm	57.1 μm	Small
40.0 μm	8.0 μm	34.3 μm	151.5 μm	Large
63.0 μm	8.0 μm	53.7 μm	227.3 μm	Large

Figure 6. Plot of the width $2\sigma_{\text{CEB}}$ of the Gaussian filter obtained from measurements of the CEB reference standards against the effective blur $2\sigma_{\text{eff}}$ resulting from different focal spot configurations. Labels are denoted as follows: reference standard (L = large, S = small)—nominal radius of assessed circle (in μm)—direction of curvature. The dotted line represents the result of a linear fit including all data points except the four for the 50 μm and 20 μm radius on the small reference standard marked by the red circle.

to be caused by the same undersampling effect that causes the increased spread in the results of the CEB method. Moreover, it has to be noted that this noise in the ITF is not actual random noise but artefacts originating from the sampling of the DFT and non-linearities of the CT system. Therefore, a correlation between the structure of the ripples has been observed in several independent measurements.

The respective values for the threshold wavelength $\lambda_{\text{PBS}}^{0.8}$ for each setting of the focal spot are summarized in table 2 together with the respective effective blur $2\sigma_{\text{eff}}$ that combines focal spot size and pixel size and the used reference standard.

4.2. Measurements

The results from the dXCT measurements of the CEB reference standards are presented in figure 6. As with the results from the simulated CT scans only valid radii, according to equation (1), are included. Similar to the simulations the

increase of $2\sigma_{\text{CEB}}$ with increasing effective blur appears linear with a slope of 0.9, but with an intersect at $2\sigma_{\text{CEB}} = -0.5$. This offset can again be explained by the inaccuracy of the effective blur calculus and the non-linearity of the reconstruction process.

The spread of the results for the different valid radii again increases with increasing effective blur from 6.1 μm at $2\sigma_{\text{eff}} = 9.8$ μm to 16.1 μm at 53.7 μm which is of similar magnitude as observed in the simulations. Only at $2\sigma_{\text{eff}} = 34.2$ μm the spread is higher with 29.4 μm. This increased spread is mainly caused by a difference between the results from the 50 μm radius on the two sizes of the reference standard. The reason for this is that the 50 μm and 20 μm radii on the small reference standard appear to be not well suited for the task because the width at the base of the structures is only about 80 μm. Therefore, the straight-line segments are rather short and not properly reproduced by the measurement leading to increased inaccuracies of the fitted radius. Another indication for these features being not suitable at this effective blur is the
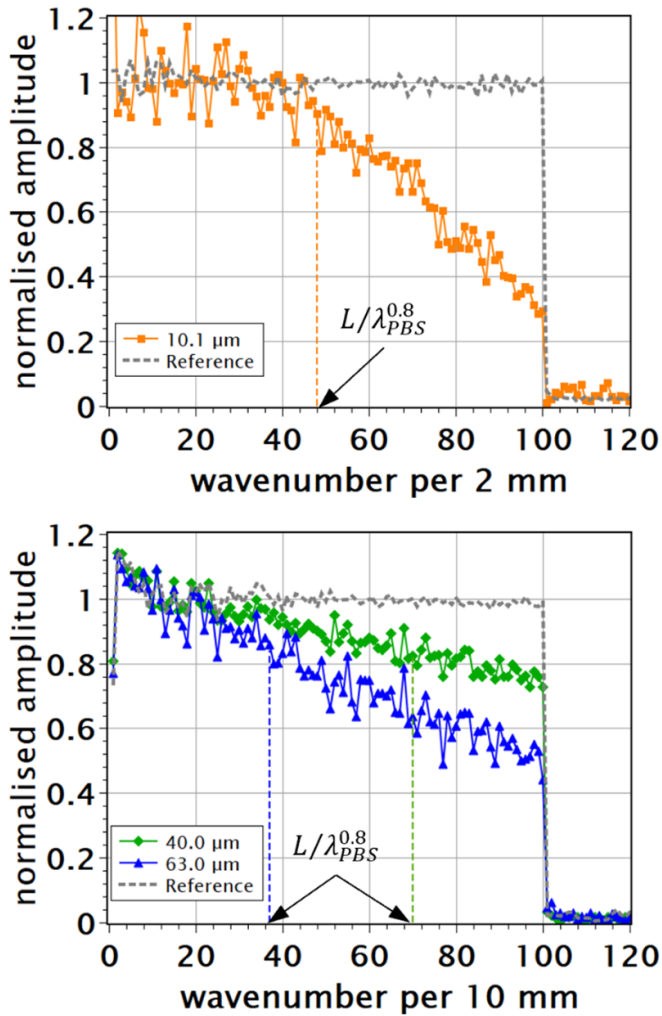
Figure 7. Plots of the ITFs obtained from measurements with different average focal spot size (10.1 μm, 40.0 μm, and 63.0 μm) of the small ($L = 2$ mm, top) and the large ($L = 10$ mm, bottom) PBS reference standards together with the result of the tactile reference measurement (dotted grey).

Table 3. Assessed threshold wavelengths for the $q = 0.8$ threshold of the ITFs obtained at the respective average focal spot size as determined with a JIMA RT RC-05 test chart together with the effective blur $2\sigma_{\text{eff}}$ and used reference standard.

Avg focal spot size (FWHM)	Voxel size	$2\sigma_{\text{eff}}$	$\lambda_{\text{PBS}}^{0.8}$	Reference standard
10.1 μm	8.0 μm	9.8 μm	41.6 μm	Small
40.0 μm	8.0 μm	34.3 μm	142.9 μm	Large
63.0 μm	8.0 μm	53.7 μm	270.3 μm	Large

smaller 0.08. This allows a direct comparison between the measurement and simulation results. The observed decrease of the normalised amplitude is similar to those observed for the simulated CT scans. However, the ITFs obtained from the dXCT-measurements are more noisy. The observed systematic and correlated ripple appear increasingly for the large PBS reference standard, when the effective focus size is larger than the voxel size. This might be connected to the inappropriate reconstruction model which assumes a point source. Additionally, as mentioned above, these measurements contain image forming artefacts like noise or beam hardening that impact the data quality. Thus, noisier ITFs than for the simulated CT scans under ideal conditions are to be expected. The ITF of the small reference standard shows particularly high noise for wavenumbers $\lesssim$45 per 2 mm. This range of the ITF is very sensitive to slight rotations, from experience in the order of 10^{-4} degrees, due to the registration of the profile and to apparent form deviations due to distortions induced by the dXCT measurement process, such as beam hardening effects that persist through the imperfect beam hardening correction.

The resulting threshold wavelengths $\lambda_{\text{PBS}}^{0.8}$ for each setting of the focal spot are listed in table 3 together with the respective effective blur and the reference standard used.

4.3. Comparison between CEB and PBS method

The single-surface MSR is calculated from the results for λ_{PBS} and σ_{CEB} obtained from simulated CT scans and dXCT measurements using the relation of equation (10) and plotted against the effective blur in figure 8. The respective values for λ_{PBS} and σ_{CEB} are summarized in table 4. The results from the two methods are in good agreement and follow a linear dependency. To compare the results to the theoretically expected dependency given by equation (10) the weights for calculating the average focal spot size from the size along the two axes of the ellipse are checked by a least-squares fit of the measured MSRs against the theory. This fit shows the smallest deviations for equal weights of 0.5 justifying the use of the arithmetic mean.

The absolute deviations between the measured MSR and the theory observed in figure 8 are within a range of ± 16 μm. For a moderate or high effective blur ($2\sigma_{\text{eff}} \gtrsim 30$ μm) this represents a relative deviation of up to 20%, whereby the relative deviation is calculated as $(\text{MSR}_{\text{meas}} - \text{MSR}_{\text{theo}})/\text{MSR}_{\text{theo}}$.

fact that in the simulation the respective fits did not converge. Therefore, those values (marked in figure 6) are excluded from the subsequent analysis.

For the subsequent comparison, again, the arithmetic means of all valid values for $2\sigma_{\text{CEB}}$ obtained at the same effective blur $2\sigma_{\text{eff}}$ is calculated to obtain the final result for that $2\sigma_{\text{eff}}$. This excludes the results from the 50 μm radius on the small reference standard marked in figure 6.

The ITFs obtained from the dXCT measurements of the PBS reference standards are plotted in figure 7 together with the ITFs of the tactile reference measurement. The tactile reference measurements show the ideal flat spatial frequency spectrum of the design with relatively low noise proving the precise manufacturing of the reference standards with very small form deviations. Comparing the frequency profiles of the tactile measurement with the one of the STL used for the simulation study shows a good agreement with deviations
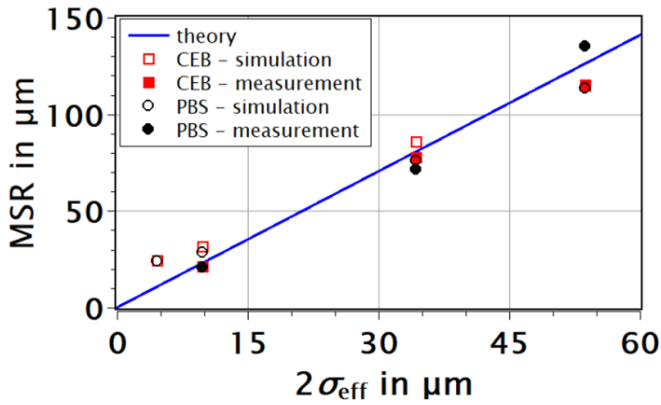
Figure 8. Plot of the MSR against the width $2\sigma_{\text{eff}}$ of the effective blur for all simulations and measurement of the PBS and CEB reference standards together with theoretically expected behaviour according to equation (10) under the assumption of an ideal Gaussian filter.

For a lower effective blur relative deviations are up to 125% although the corresponding absolute deviations are not the highest observed with only up to 13 µm.

The most likely explanation for these higher relative deviations is that the filtering of the CT system does not exactly follow the model assumption of a Gaussian filter and other effects influencing the MSR are not considered in the calculation of the effective blur, e.g. limited number of projections, movement of the focal spot (measurement only), shape of the focal spot (except simulation of point source), CT reconstruction filter, instabilities of the CT geometry like a 'wobbling' of the rotation axis (measurement only), or limited single-float precision (simulations only). The influence of such effects is independent of the focal spot size and the pixel size and causes absolute deviations within a similar range for all values of $2\sigma_{\text{eff}}$. Consequently, their relative contribution is much larger at a small effective blur. This also means that the MSR cannot become infinitely small but reaches a minimum at high magnifications and small focal spot sizes. It cannot be reduced further only by decreasing the focal spot size or pixel size.

Moreover, the deviations appear random and there is no obvious bias between the results of both methods. This can be corroborated by a one-sample Student's t-test [10]. For this the null hypothesis H_0 is formulated as follows: The deviations between measured MSR and theoretical MSR at a given $2\sigma_{\text{eff}}$ are zero. The corresponding alternative hypothesis H_1 is: The deviations between the measured MSR and the theoretical MSR are not zero. The mean value for the deviations between measured and theoretical MSR across all data points in figure 8 is $\overline{\Delta\text{MSR}} = 0.93\,\mu\text{m}$ with a standard deviation of $\sigma_{\Delta\text{MSR}} = 11.62\,\mu\text{m}$. For the given 13° of freedom this results in a t-value of $t = 0.41$ and a two-tailed p-value of $p = 0.69$. This is much larger than the commonly used level of significance of $\alpha = 0.05$ and the null hypothesis cannot be rejected. While this analysis does not take the measurement uncertainty into account which could not yet be determined, it strongly indicates that the measurement and simulation results

Table 4. Summary of results for half of the threshold wavelength $1/2\lambda_{\text{PBS}}$ and standard deviation of the Gaussian filter σ_{CEB} together with the ratio between the two quantities for each measurement and simulation.

	$2\sigma_{\text{eff}}$	$1/2\lambda_{\text{PBS}}$	σ_{CEB}	Ratio
Simulation	4.6 µm	23.8 µm	5.2 µm	4.57
	9.8 µm	28.6 µm	6.7 µm	4.27
	34.3 µm	75.8 µm	18.3 µm	4.59
	53.7 µm	113.7 µm	24.4 µm	4.66
Measurement	9.8 µm	20.8 µm	4.5 µm	4.62
	34.3 µm	71.5 µm	16.5 µm	4.33
	53.7 µm	135.2 µm	24.5 µm	5.52

are random samples from a population that follows the presented theoretical dependency between the MSR and $2\sigma_{\text{eff}}$.

Similarly, a Welch's test [11] was used to judge whether there is a difference in the deviations to the theoretical MSR between the PBS and CEB method. The mean values of the deviations are $\overline{\Delta\text{MSR}_{\text{PBS}}} = -0.18\,\mu\text{m}$ and $\overline{\Delta\text{MSR}_{\text{CEB}}} = 0.04\,\mu\text{m}$ with standard deviations $\sigma_{\Delta\text{MSR}_{\text{PBS}}} = 9.57\,\mu\text{m}$ and $\sigma_{\Delta\text{MSR}_{\text{CEB}}} = 9.63\,\mu\text{m}$ for the PBS and CEB method respectively. Performing the Welch t-test gives a t-value of $t = 0.04$ and a two-tailed p-value of $p = 0.97$. Therefore, it is very likely the two methods yield the same result for the MSR and differences a purely random.

Another way of comparing the experimental results to the theory is to calculate an empirical factor relating $1/2\lambda_{\text{PBS}}$ to σ_{CEB} and compare this to the factor predicted by equation (10). To calculate the empirical factor the ratio $\lambda_{\text{PBS}}/2\sigma_{\text{CEB}}$ is calculated for each pair of results from measurements and simulations with identical settings for the focal spot. These ratios are summarized in table 4.

The arithmetic mean of these ratios yields an average empirical factor of 4.65 which agrees very well with the theoretical factor of 4.70 to further corroborate the relation presented in equation (10). However, the results of the ratio for the individual measurements and simulations show a significant spread of $+0.82$ to -0.43 (values compared to the theoretical factor 4.70). This indicates that, while the results of the two methods are equivalent and agree well with the theory, the uncertainty of the obtained MSR values is rather large. However, evaluation of the uncertainty of these measurements and ways to reduce it are topics for further research.

5. Summary

The experimental comparison of the PBS and CEB methods for the characterization of the MSR shows that the results obtained from the two methods are consistent with each other and follow an analytical relation. This relation was derived under the model assumption of a Gaussian filter for the CEB method and allows to calculate consistent MSR values from the respective immediate results λ_{PBS} and σ_{CEB} of each method.

Furthermore, a simulation study and dXCT measurements performed on differently sized reference standards also show that the two methods yield equivalent results. Variations between the two different methods are of similar magnitude as variations of the results from each method alone.

Deviations to the results expected from theory are mostly within the span of the results obtained from simulations and measurements. Larger deviations to the theory are observed for small focal spot sizes, where the model assumptions used for the calculation of the effective blur are assumed to be not valid anymore.

Data availability statement

The data cannot be made publicly available upon publication because no suitable repository exists for hosting data in this field of study. The data that support the findings of this study are available upon reasonable request from the authors.

Acknowledgments

ORCID iDs

René Laquai ⬤ https://orcid.org/0000-0003-4932-1748
Ulrich Neuschaefer-Rube ⬤ https://orcid.org/0000-0002-5122-8799

References

[1] JCGM 200:2012 2012 *International Vocabulary of metrology—Basic and General Concepts and Associated Terms (VIM)* (Sèvres Cedex: Joint Committee for Guides in Metrology)

[2] Zanini F and Carmigniato S 2017 Two-spheres method for evaluating the metrological structural resolution in dimensional computed tomography *Meas. Sci. Technol.* **28** 114002

[3] Illemann J, Bartscher M, Jusko O, Härtig F, Neuschaefer-Rube U and Wendt K 2014 Procedure and reference standard to determine the structural resolution in coordinate metrology *Meas. Sci. Technol.* **25** 064015

[4] Bartscher M, Neuschaefer-Rube U, Illemann J, Borges de Oliveira F, Stolfi A and Carmignato S 2018 Qualification and testing of CT systems *Industrial X-ray Computed Tomography* ed S Carmignato, W Dewulf and R Leach (Cham: Springer)

[5] Illemann J 2020 Tracable measurement of the instrument transfer function in dXCT *10th Conf. on Industrial Computed Tomography (Wels)*

[6] Thomsen-Schmidt P 2011 Characterization of a traceable profiler instrument for areal roughness measurement *Meas. Sci. Technol.* **22** 094019

[7] Bellon C, Jaenisch G-R and Deresch A 2016 Combining analytical and Monte Carlo modelling for industrial radiology *19th World Conf. on Non-Destructive Testing (Munich)*

[8] Weisstein E W Gaussian function *From MathWorld–A Wolfram Web Resource* (available at: https://mathworld.wolfram.com/GaussianFunction.html)

[9] Illemann J, Meinel D and Bellon C 2019 Effektive Bestimmung der Fokusparameter von Mikrofokus-Röntgenquellen *DACH-Jahrestagung 2019 (Garmisch-Partenkirchen)*

[10] Student 1908 The probable error of a mean *Biometrika* **6** 1–25

[11] Welch B L 1947 The generalization of 'STUDENT'S' problem when several different population variances are involved *Biometrika* **34** 28–35